Turbulence Control Simulation using the Variational Multiscale Method*

Srinivas Ramakrishnan,†
S. Scott Collis,‡§
Rice University
Houston, Texas 77005-1892

Abstract

The capabilities of the variational multiscale (VMS) method are explored in the context of turbulence control by applying VMS to the simulation of a simple opposition-control strategy for turbulent channel-flow with the results compared to prior Direct Numerical Simulations (DNS) and Large-Eddy Simulations (LES) based on the dynamic subgrid-scale model. In all cases, the VMS method is found to be more efficient and more accurate than the dynamic model and the simplicity, accuracy, and generality of VMS makes it particularly attractive for turbulence control investigations.

Nomenclature

C_s	Smagorinisky coefficient
$\mathcal{D}$	drag
k	wave number, $k = 2\pi/\lambda$
L	length
N	number of modes and partition size
p	pressure
$\mathcal{P}_{\mathcal{D}}$	power saved due to drag reduction
$\mathcal{P}_{\phi}$	power input due to control
$\mathcal{P}_{\lvert\phi\rvert}$	power input due to control (conservative)
P	perimeter of the space-time domain
Q	space-time domain, $\mathsf{Q} = \Omega \times [0, T]$
r	pressure weighting function

*Presented at the 1^{st} AIAA Flow Control Conference, June 24-26, 2002 as AIAA paper 2002-3280
†Ph.D. Candidate, Mechanical Engineering and Materials Science, seenu@rice.edu
‡Assistant Professor, Mechanical Engineering and Materials Science, member AIAA.
§Current affiliation: Sandia National Laboratories, Senior Member of Tehcnical Staff, Optimization and Uncertainty Estimation, sscoll@sandia.gov

Re_τ	turbulence Reynolds number $Re_\tau = u_\tau \delta / \nu$
t	time
T	time interval
$\boldsymbol{u}$	velocity vector, $\boldsymbol{u} = \{u, v, w\}^{\mathcal{T}}$
u	velocity component in the x-direction
u_τ	friction velocity $u_\tau = \sqrt{\tau_w / \rho}$
v	velocity component in the y-direction
w	velocity component in the z-direction
$\boldsymbol{x}$	coordinate vector, $\boldsymbol{x} = \{x, y, z\}^{\mathcal{T}}$
x	streamwise coordinate
y	wall-normal coordinate
y_s^+	sensing plan location in wall units
z	spanwise coordinate
$\boldsymbol{U}$	state vector $\boldsymbol{U} = \{\boldsymbol{u}, p\}^{\mathcal{T}}$
$\mathcal{V}$	solution function space
$\boldsymbol{w}$	velocity weighting-function
$\boldsymbol{W}$	state weighting-function
$\mathcal{W}$	test function space
λ	wave length
δ	channel half-height
Δ	length scale
Γ	boundary of Ω
ν	kinematic viscosity
Ω	spatial domain
ρ	density
τ_w	average wall shear-stress

Modifiers

$\overline{(\,)}$	large scales
$\widetilde{(\,)}$	small scales
$\widehat{(\,)}$	unresolved scales
$+$	wall units
$\Delta(\,)$	change in a quantity
rms	root mean square
x, y, z	coordinate direction
$\mathcal{T}$	transpose

Introduction

This paper extends our research to develop improved methods for simulation of turbulence control using Large-Eddy Simulation (LES). The LES based methods presented here exploit the promise of the variational multiscale model to improve the efficiency of control formulations applied to turbulent flows. Our prior work [1] has demonstrated that LES with the dynamic subgrid-scale model is an effective tool for studying turbulence control of wall-bounded flows. However, the well-known difficulties in extending the dynamic model to inhomogeneous flows limits applications to more complex turbulence control problems. Likewise, the algebraic complexity of the dynamic procedure makes application of gradient based optimal control strategies cumbersome. Recently a new approach to LES called the Variational Multi-Scale (VMS) method [2] has been introduced that demonstrates results equal or superior to the dynamic model for both equilibrium and non-equilibrium turbulent channel flows [3]. In addition, the VMS method can be readily extended to complex geometries (see [4] for one example), since scale separation is effected through projection instead of spatial filtering as employed in traditional LES [2]. The resulting model equations are also very simple, making the approach attractive for gradient-based optimal control. In this paper, we explore the viability of the VMS method to serve as an efficient and accurate tool in the context of turbulence control by applying VMS to the simulation of a simple opposition control strategy for turbulent channel flow with the results compared to prior DNS and LES. The objective of this research is to determine if the advantages of VMS reported for uncontrolled flows also extend to controlled turbulent flows.

Although the potential of turbulence control to improve the performance of aerospace applications is significant, turbulence control is a cutting-edge technology with a number of important engineering challenges that must be overcome before practical systems become viable. These challenges are non-trivial and include such issues as mechanical losses, actuator/sensor design, weight, maintainability, and cost. Likewise, fundamental issues associated with the flow physics, modeling, and control mechanisms are also in need of further research. It is for these reasons that simulation tools, such as the VMS methods discussed here, are needed to evaluate and optimize different control strategies long before committing them to hardware.

The paper begins with a brief review of opposition control followed by an introduction to the VMS method. We briefly summarize the results from uncontrolled VMS simulations along with comparisons to DNS and the dynamic model in order to validate our implementation. Our VMS implementation is then used to study opposition control across a range of Reynolds numbers and comparisons are made to prior DNS and LES results.

Review of Opposition Control

Opposition control (also called "out-of-phase" control) is a conceptually simple feedback control strategy that introduces control in the form of distributed suction and blowing at the wall surface in an attempt to oppose the motion of near-wall turbulent structures. The physical argument used to motivate this strategy is demonstrated in Figure 1. Near-wall turbulent structures generally take the form of streamwise oriented counter-rotating vortices (see e.g., [5–7]). By sensing the vertical component of velocity at a sensing plane located a distance y_s^+ from the wall and using suction/blowing in opposition to the measured velocity, one hopes to attenuate the motion of turbulent structures thereby reducing the transport of high momentum fluid toward the wall and reducing drag. Doing so may also hamper the cycle of near-wall turbulence generation [8]. Evidence to support this heuristic description of opposition control is supplied by the LES flow visualization shown in Figure 2. This figure highlights near-wall turbulent structures for both an uncontrolled and opposition controlled flow at $Re_\tau = 180$ using an iso-surface of the second largest eigenvalue of the velocity gradient tensor which has been shown to be an effective indicator of coherent vortical structures in turbulent shear flows [7]. Clearly the number of structures is reduced in the controlled flow and a similar effect is seen in flow visualizations from DNS [9], albeit with greater fine-scale structure visible.

While the origin of opposition control is somewhat uncertain [10], the first simulations demonstrating this method are those of [11] who used DNS at $Re_\tau = 180$ reporting about 20% drag reduction when the sensing plane is located at $y_s^+ = 10$. The more recent DNS by [9] shows that, again for $Re_\tau = 180$, the optimal sensing plane location is $y_s^+ \approx 15$ which gives about 25% drag reduction. Both studies reveal that drag increases when the control is set to counter motions too far from the wall, say at $y_s^+ > 25$ [9, 11]. These DNS studies serve to demonstrate the effectiveness of opposition control as well as identify likely mechanisms for drag reduction when using opposition control. In so doing, they spurred on a number of other investigations that built on the idea of opposition control in a variety of ways (see [1] for a review). In particular, the experience gained from opposition control has played an important role in interpreting the effects of more complex control strategies such as neural networks [12] and optimal control [13]. Unfortunately, most, if not all, prior studies of opposition control and related control strategies have been performed at very low turbulence Reynolds numbers, $Re_\tau < 200$. Recently, the authors [1] have utilized LES with the dynamic subgrid-scale model to explore the influence of viscous effects on opposition control of low Reynolds number channel flows. This study revealed that both the effectiveness and efficiency of opposition control are reduced as Reynolds number increases. While the dynamic model has proven to be an accurate and efficient tool for exploring turbulence control for wall bounded flows using both opposition and optimal control strategies [1, 14–16], the dynamic model does, however, suffer from a number of disadvantages that limit its application to more complex flows. To ad-

dress these limitations, this paper presents the first application of the variational multiscale (VMS) method of turbulence modeling to turbulence control simulations. Before presenting results using this new formulation, we first briefly review the VMS method.

Review of Variational Multiscale Method

The Variational Multiscale (VMS) method for Large-Eddy Simulation (LES) was first described by Hughes, Mazzei, and Jansen [2] and recently clarified by Collis [17]. Following the discussion in Collis [17], the strong form of the Navier-Stokes equations for incompressible flows are

$$\mathcal{N}(\boldsymbol{U}) \equiv \left\{ \begin{array}{c} \frac{\partial \boldsymbol{u}}{\partial t} + \nabla \cdot (\boldsymbol{u} \otimes \boldsymbol{u}) + \nabla p - \nu \Delta \boldsymbol{u} \\ \nabla \cdot \boldsymbol{u} \end{array} \right\} = \left\{ \begin{array}{c} \mathbf{f} \\ \psi \end{array} \right\} \equiv \boldsymbol{F}, \tag{1}$$

where $\boldsymbol{u}$ is the velocity vector, p is the pressure, ν is the kinematic viscosity (or, the inverse of the Reynolds number if non-dimensional, $\mathbf{f}$ is a body force and ψ is volumetric source, and $\otimes$ denotes the tensor product $(\boldsymbol{u} \otimes \mathbf{v})_{ij} = u_i v_j$. Equations (1) are solved subject to appropriate boundary conditions and initial conditions.

The fixed spatial domain for the problem is denoted by Ω with boundary $\Gamma = \partial\Omega$. The time interval of interest is $[0, T]$ so that the space-time domain is $\mathsf{Q} = \Omega \times [0, T]$ with lateral boundary $\mathsf{P} = \Gamma \times [0, T]$. The state vector, $\boldsymbol{U} \equiv \{\boldsymbol{u}, p\}^{\mathcal{T}}$ is defined on the closure of the space-time domain $\overline{\mathsf{Q}}$ and is in the function space $\mathcal{V}$. Details regarding the appropriate function space for incompressible Navier–Stokes solutions can be found in [18, 19]

A variational form of the Navier–Stokes equations is constructed by introducing another function space, $\mathcal{W}$, of test functions $\boldsymbol{W} \equiv \{\boldsymbol{w}, r\}^{\mathcal{T}} \in \mathcal{W}$. The function space $\mathcal{W}$ is the same as $\mathcal{V}$ except that the components of $\boldsymbol{W}$ are zero anywhere that a Dirichlet boundary condition applies on $\boldsymbol{U}$. The variational form of the equations are obtained by taking the inner product of test functions $\boldsymbol{W}$ with (1) and integrating over the space-time domain, Q, where the inner product is defined as

$$(\mathbf{f}, \mathbf{g})_{\mathsf{Q}} \equiv \int_{\mathsf{Q}} \mathbf{f} \cdot \mathbf{g} \, d\mathsf{Q}. \tag{2}$$

This leads to the variational form of the Navier-Stokes equations,

$$B(\boldsymbol{W}, \boldsymbol{U}) = (\boldsymbol{W}, \mathcal{N}(\boldsymbol{U}))_{\mathsf{Q}} = (\boldsymbol{W}, \boldsymbol{F})_{\mathsf{Q}} \quad \forall \, \boldsymbol{W} \in \mathcal{W}, \tag{3}$$

where $B(\boldsymbol{W}, \boldsymbol{U})$ is defined as

$$\begin{aligned} B(\boldsymbol{W}, \boldsymbol{U}) &= \left(\boldsymbol{w}, \frac{\partial \boldsymbol{u}}{\partial t} \right)_{\mathsf{Q}} - (\nabla \boldsymbol{w}, \boldsymbol{u} \otimes \boldsymbol{u})_{\mathsf{Q}} - (\nabla \cdot \boldsymbol{w}, p)_{\mathsf{Q}} + (\nabla^s w, 2\nu \nabla^s \boldsymbol{u})_{\mathsf{Q}} \\ &+ (r, \nabla \cdot \boldsymbol{u})_{\mathsf{Q}} + (\boldsymbol{w}, \boldsymbol{n} \cdot (\boldsymbol{u} \otimes \boldsymbol{u}))_{\mathsf{P}} + (\boldsymbol{w}, p\boldsymbol{n})_{\mathsf{P}} - (\boldsymbol{w}, 2\nu \nabla^s \boldsymbol{u} \cdot \boldsymbol{n})_{\mathsf{P}} \,, \end{aligned} \tag{4}$$

$\nabla^s \boldsymbol{u}$ is the strain-rate tensor, i.e. $(\nabla^s \boldsymbol{u})_{ij} = (u_{i,j} + u_{j,i})/2$), and $\boldsymbol{n}$ is the outward unit normal vector on the boundary Γ. Integration by parts has been applied to the viscous, convection, and pressure-gradient terms generating appropriate fluxes on the spatial boundaries.

The variational multiscale method is built around the idea of *a priori* scale separation where we utilize a three-scale partition [17] that highlights the role of unresolved scales. Thus, the large scales are denoted as $\overline{\boldsymbol{U}}$, the small scales as $\widetilde{\boldsymbol{U}}$, and the unresolved scales as $\widehat{\boldsymbol{U}}$, so that the solution and weighting function spaces are partitioned as

$$\mathcal{V} = \overline{\mathcal{V}} \oplus \widetilde{\mathcal{V}} \oplus \widehat{\mathcal{V}}\,, \qquad \mathcal{W} = \overline{\mathcal{W}} \oplus \widetilde{\mathcal{W}} \oplus \widehat{\mathcal{W}} \tag{5}$$

and the solution and weighting functions can be written as

$$\boldsymbol{U} = \overline{\boldsymbol{U}} + \widetilde{\boldsymbol{U}} + \widehat{\boldsymbol{U}}\,, \qquad \boldsymbol{W} = \overline{\boldsymbol{W}} + \widetilde{\boldsymbol{W}} + \widehat{\boldsymbol{W}}\,. \tag{6}$$

As shown in Ref. [17] the exact equations for each scale range are identified by the particular partition of the weighting function that appears in the first slot of operator $B(\boldsymbol{W}, \boldsymbol{U})$ in equation (4). Thus, the exact large, small, and unresolved equations are given by

$$\text{Large} \qquad B(\overline{\boldsymbol{W}}, \overline{\boldsymbol{U}} + \widetilde{\boldsymbol{U}} + \widehat{\boldsymbol{U}}) = (\overline{\boldsymbol{W}}, \boldsymbol{F})_{\mathsf{Q}}, \tag{7}$$

$$\text{Small} \qquad B(\widetilde{\boldsymbol{W}}, \overline{\boldsymbol{U}} + \widetilde{\boldsymbol{U}} + \widehat{\boldsymbol{U}}) = (\widetilde{\boldsymbol{W}}, \boldsymbol{F})_{\mathsf{Q}}, \tag{8}$$

$$\text{Unresolved} \qquad B(\widehat{\boldsymbol{W}}, \overline{\boldsymbol{U}} + \widetilde{\boldsymbol{U}} + \widehat{\boldsymbol{U}}) = (\widehat{\boldsymbol{W}}, \boldsymbol{F})_{\mathsf{Q}}. \tag{9}$$

At this point, it is convenient to introduce definitions of the Reynolds-stress projection and cross-stress projections [17]. The projection of the unresolved Reynolds stress onto the large scales is defined as

$$R(\overline{\boldsymbol{w}}, \widehat{\boldsymbol{u}}) = (\nabla \overline{\boldsymbol{w}}, \widehat{\boldsymbol{u}} \otimes \widehat{\boldsymbol{u}})_{\mathsf{Q}} - (\overline{\boldsymbol{w}}, \boldsymbol{n} \cdot (\widehat{\boldsymbol{u}} \otimes \widehat{\boldsymbol{u}}))_{\mathsf{P}}. \tag{10}$$

Likewise, the projection of the large/unresolved cross-stresses onto the large scales is defined as

$$C(\overline{\boldsymbol{w}}, \overline{\boldsymbol{u}}, \hat{\boldsymbol{u}}) = (\nabla \overline{\boldsymbol{w}}, \overline{\boldsymbol{u}} \otimes \widehat{\boldsymbol{u}} + \widehat{\boldsymbol{u}} \otimes \overline{\boldsymbol{u}})_{\mathsf{Q}} - (\overline{\boldsymbol{w}}, \boldsymbol{n} \cdot (\overline{\boldsymbol{u}} \otimes \widehat{\boldsymbol{u}} + \widehat{\boldsymbol{u}} \otimes \overline{\boldsymbol{u}}))_{\mathsf{P}}. \tag{11}$$

With this notation, the equations for the *resolved scales*, denoted by $\overline{\widetilde{\boldsymbol{U}}} = \overline{\boldsymbol{U}} + \widetilde{\boldsymbol{U}}$, can be written as

$$B(\overline{\widetilde{\boldsymbol{W}}}, \overline{\widetilde{\boldsymbol{U}}}) = (\overline{\widetilde{\boldsymbol{W}}}, \boldsymbol{F})_{\mathsf{Q}} + \underbrace{R(\overline{\boldsymbol{w}}, \widehat{\boldsymbol{u}}) + C(\overline{\boldsymbol{w}}, \overline{\widetilde{\boldsymbol{u}}}, \widehat{\boldsymbol{u}}) + R(\widetilde{\boldsymbol{w}}, \widehat{\boldsymbol{u}}) + C(\widetilde{\boldsymbol{w}}, \overline{\widetilde{\boldsymbol{u}}}, \widehat{\boldsymbol{u}})}_{\text{need to model}}. \tag{12}$$

Solving just this equation for the resolved scales ($\forall\, \overline{\widetilde{\boldsymbol{W}}} \in \overline{\widetilde{\mathcal{W}}}$) requires that the terms depending on

the unresolved scales be modeled. Thus, the modeled Navier–Stokes equations are

$$B(\overline{\widetilde{\boldsymbol{W}}}, \overline{\widetilde{\boldsymbol{U}}}) = (\overline{\widetilde{\boldsymbol{W}}}, \boldsymbol{F})_{\mathsf{Q}} + \overline{M}(\overline{\boldsymbol{W}}, \overline{\widetilde{\boldsymbol{U}}})_{\mathsf{Q}} + \widetilde{M}(\widetilde{\boldsymbol{W}}, \overline{\widetilde{\boldsymbol{U}}})_{\mathsf{Q}} \tag{13}$$

where $\overline{M}$ and $\widetilde{M}$ denote the model terms acting on the large and small scales, respectively. Since the goal of large eddy simulation is to accurately predict the evolution of the largest scales of motion, it is desirable that there be no direct model acting on the large-scales. Thus we set $\overline{M}(\overline{\boldsymbol{W}}, \overline{\widetilde{\boldsymbol{U}}})_{\mathsf{Q}} = 0$ and it is argued in [17] that this is reasonable as long as there is sufficient scale separation between the large and unresolved scales i.e. a sufficiently large small-scale partition. Results demonstrating the significance of the small-scale partition in enforcing adequate scale separation can be found in [20]. Conversely, the influence of the unresolved scales on the small-scales must be modeled and, following [2], we utilize a simple constant coefficient Smagorinsky model acting on the small-scales

$$\widetilde{M}(\widetilde{\boldsymbol{W}}, \overline{\widetilde{\boldsymbol{U}}})_{\mathsf{Q}} = (\boldsymbol{\nabla}^s \widetilde{\boldsymbol{w}}, 2(C_S \widetilde{\Delta})^2 \, |\boldsymbol{\nabla}^s \widetilde{\boldsymbol{u}}| \, \boldsymbol{\nabla}^s \widetilde{\boldsymbol{u}})_{\mathsf{Q}} \tag{14}$$

where C_S is the constant Smagorinsky coefficient, $|\boldsymbol{\nabla}^s \widetilde{\boldsymbol{u}}|$ is the norm of the small-scale strain-rate tensor, and $\widetilde{\Delta} = (\Delta x \Delta y \Delta z)^{1/3}$ is a representative length scale for the small scales.

Since the large-scales have no direct model, when all scales of motion fall within the large partition, the exact solution (i.e. DNS) is obtained. This feature is missing from classical LES and RANS methods. Likewise, at finite resolution when both large and small scales are active, it is likely that the large scales will be more accurate and this is verified in recent studies [3, 20, 21]. In summary, the VMS approach provides a number of advantages over other LES models including:

- the variational formulation provides a solid mathematical foundation for turbulence modeling [2, 4, 17];
- the VMS approach, with an appropriate numerical method [4], can be readily extended to complex geometries – there are no commutativity or homogeneity issues like those that arise when using spatial filters (see *e.g.*, [2, 22]);
- a constant coefficient Smagorinsky type model acting only on small scales has been shown to be effective, even for wall bounded flows [3, 21];
- the modeled equations are considerably simpler then the dynamic subgrid-scale model [23, 24] making calculations potentially more efficient.

We believe that these benefits may prove to be particularly valuable for simulation of turbulence control systems which motivates our current application of VMS to opposition control for turbulent channel flow.

Problem Formulation and Implementation

We now focus specifically on incompressible, fully-developed turbulent flow in a planar channel where the fluid motion is predicted using LES with a VMS model. In the following discussion the coordinate system for the channel flow is x in the streamwise direction, y in the wall-normal direction, and z in the spanwise direction. The flow in the streamwise and spanwise directions is assumed to be periodic with the box-size set to ensure that the turbulence is decorrelated.

VMS has been implemented in our existing LES flow solver that uses a hybrid Fourier-spectral and finite-volume method [25, 26] which has been modified to run efficiently on workstation class computers and shared memory parallel computers [16]. Given that the spanwise and streamwise directions are homogeneous for planar channel flow, a dealiased Fourier-Galerkin method is the natural choice. In the LES/DNS literature, spectral methods are also commonly used in the wall-normal direction for channel flows, based on either Chebyshev [27] or Legendre [28] polynomials. In fact, the recent VMS study of Hughes et al. [3] utilized a Legendre-Galerkin method in the wall-normal direction. Typically these fully spectral methods for channel flows treat the convective terms explicitly in time to prevent the need to solve large, dense non-linear systems of equations. However, in turbulence control studies, the combination of non-zero wall-normal velocity and the highly refined meshes required in the near-wall region lead to a stringent convective stability constraint when using explicit time-advancement. It is for this reason that we use a conservative second-order finite-volume method on a staggered grid with fully implicit Crank-Nicholson time-advancement in the wall-normal direction that leads to an efficient implementation which only requires the solution of tri-diagonal systems of equations. In the homogeneous directions, an explicit, third-order accurate Runge-Kutta method is utilized and a fractional-step algorithm is used to enforce incompressibility. See [16] for details.

Since we use a Fourier-spectral method in x and z based on a Galerkin variational formulation, it is straightforward to apply the VMS scale separation in these directions as described above. However, since a finite-volume method is used in the wall-normal direction, the application of scale separation in that direction is inconvenient. Therefore, in an approach we call planar VMS (hereafter called PVMS), analogous to the common practice of filtering only in the planes [23, 24], we apply scale separation only in the planes. Thus, the small-scales are defined through variational projection of the Fourier basis only in the (x, z) planes. An important parameter of any VMS method is the choice of partition between large and small scales. With a Fourier series representation in the planes, our numerical solutions take the form

$$\boldsymbol{U}(\boldsymbol{x}, t) = \sum_{k_x=-N_x/2}^{N_x/2-1} \sum_{k_z=-N_z/2}^{N_z/2-1} \boldsymbol{U}(y, t; k_x, k_z) e^{i(k_x x + k_z z)}$$

where N_x and N_z are the number of Fourier modes in the resolved scales in the streamwise and spanwise directions, respectively. The large/small partition is accomplished by defining the partitions $\overline{N}_x$ and $\overline{N}_z$ such that the large scales are

$$\overline{\boldsymbol{U}}(\boldsymbol{x},t) = \sum_{k_x=-\overline{N}_x/2}^{\overline{N}_x/2-1} \sum_{k_z=-\overline{N}_z/2}^{\overline{N}_z/2-1} \boldsymbol{U}(y,t;k_x,k_z) e^{i(k_x x + k_z z)}$$

with all remaining scales in the small partition. In cases where the same partition is used in x and z we define $\overline{N} = \overline{N}_x = \overline{N}_z$.

Note that other applications of VMS to channel flows reported in the literature, Hughes *et al.* [3] and Oberai and Hughes [21], used a Fourier-Galerkin method in the homogeneous directions with a Legendre-Galerkin method in the wall-normal direction so that the VMS method could be applied in all three coordinate directions. Their work demonstrates that the VMS method results in high quality solutions that are often superior to the dynamic model, especially for transient turbulent flows. We reiterate that this approach is not convenient for turbulence control simulations and we show in the next section that our planar implementation yields results similar in quality to the full VMS method of Hughes *et al.* [3].

Results

The domain sizes and grid resolutions used to validate our planar implementation of VMS are given in Table 1. Similarly, the domain sizes and grid resolutions for all PVMS simulations used in the control study are presented in Table 2. In both tables, the grid spacings Δx^+ and Δz^+ are computed based on the mesh prior to dealiasing while Δy_w^+ and Δy_c^+ are the y-resolution at the wall and centerline of the channel, respectively. The Smagorinsky coefficient $C_s = 0.1$ for all PVMS simulations. All dynamic model results presented here use our implementation of the dynamic subgrid-scale model in the same code [16] and simulation parameters for the dynamic model are presented in Table 3. To distinguish simulations at the same Reynolds number with varying parameters, we include a case number associated with each simulation (see Tables 2 and 3). For the same Reynolds number, increasing case number generally means a higher resolution. We choose δ, the channel half height, as the reference length scale and $u_\tau = (\tau_w/\rho)^{1/2}$ as reference velocity scale, where τ_w is the average shear-stress on the walls. The reference (convective) time-scale is then δ/u_τ and the reference Reynolds number is $Re_\tau = u_\tau \delta/\nu$. In presenting results, we sometimes report viscous time-units which are defined as $t^+ = t u_\tau^2/\nu$.

Appropriate partition selection $(\overline{N})$ is vital for the success of VMS and, in particular, the partition must be commiserate with the assumptions made in deriving the VMS model equations. The large-scale space is selected to sufficiently represent the dynamically important large scales in the flow. We show in a companion work [20, 29] that for turbulent channel flow, the large-scale space

must be sufficient to capture scales half the size of the typical near-wall streaks ($\bar{\lambda}_z^+ \approx 50$ and $\bar{\lambda}_x^+ \approx 200$). With the large-scale space set, the small scales are determined by the resolution limit and the small-scale space must provide sufficient scale separation between the unresolved (subgrid) scales and the large scales. This minimizes the direct influence of the unresolved scales on the large scales which is an important assumption in deriving the model equations for VMS [17]. We use this approach as a guide in selecting both the partition between large and small scales and the resolution limit. In the results that follow, we demonstrate the influence of both partition and resolution on the quality of the simulations. The interested reader is directed to refs. [20, 29] for details.

Uncontrolled Flow

We begin by presenting quantitative comparisons of low-order statistics for fully-developed turbulent channel-flow at $Re_\tau = 180$ using PVMS, the dynamic model, and DNS. All simulations at this Reynolds number use the domain size $(2\pi, 2, 4\pi/3)$ which matches that used by the full VMS study of Hughes *et al.* [3]. For PVMS, we use the same number of Fourier modes in the streamwise and spanwise directions as Hughes *et al.* [3] However, initially the number of grid points in the wall-normal direction is set to twice the number of Legendre modes used by Hughes *et al.* [3] to account for our second-order method as opposed to their spectral discretization. This increase in resolution was deemed sufficient based our prior experience with the dynamic model [1, 16] for the same conditions and numerical method (we also perform a resolution study below). Thus, PVMS and dynamic model use a resolution of $32 \times 65 \times 32$ (see Table 1) while the DNS calculation uses a resolution of $80 \times 129 \times 96$. Mean and rms velocity profiles for all three methods are shown in Fig. 3 where the PVMS uses the partition $\overline{N} = 14$. The PVMS mean-flow profile in Fig. 3(a) is in excellent agreement with DNS (they cannot be distinguished at this scale), while the dynamic model for the same resolution slightly over predicts the wall shear-stress. The rms velocities, shown in Fig. 3($b - d$), for both PVMS and the dynamic model are in good agreement with unfiltered DNS.

Figure 4 shows the effect of reducing the wall-normal resolution from 65 to 33 nodes demonstrating that the mean-velocity profiles from PVMS are insensitive to the decrease in wall-normal resolution. Also included in this figure are results from a coarse grid "DNS" computed at the resolution $32 \times 65 \times 32$. This coarse "DNS" significantly over predicts the shear stress at the wall demonstrating the need for a subgrid-scale model at this resolution. Figure 5 shows a similar comparison for rms velocities, where, again, the PVMS simulations are in good agreement with the unfiltered DNS while the coarse "DNS" shows significant deviation from the reference DNS. In particular, the location of the peak in the streamwise turbulence intensity (u_{rms}) is accurately predicted by the PVMS simulations while the peak predicted by coarse "DNS" is shifted towards

the wall. Although we initially used a rather high wall-normal resolution (65 grid points) to make up for our use of a second-order method as compared to the spectral method used by Hughes *et al.* [3], these results demonstrate that PVMS is relatively insensitive to wall-normal resolution. PVMS using the same resolution as Hughes *et al.* [3] (albeit with a second-order method in y) leads to results in good agreement with DNS.

Since the partition between large and small scales is an important parameter in VMS simulations, Figures 6 and 7 shown the influence of small changes in the partition location for both mean and rms velocity profiles. While the partition $(\overline{N})$ does influence the solution, minor departures from the nominal partition do not lead to significant differences. In fact, these changes can be partially offset by changes in the value of C_s (recall we have fixed $C_s = 0.1$) and this is explored further in refs. [20, 29]. Simulations at higher friction velocity Reynolds numbers exhibit a similar behavior (see [29]) and these observations are consistent with those reported by Hughes *et al.* [3] and by Oberai and Hughes [21].

Moving on to higher Reynolds numbers, PVMS results at $Re_\tau = 590$ are now compared with the dynamic model and DNS [30]. The partition for this Reynolds number, using a resolution of $72 \times 149 \times 72$ is $\overline{N} = 26$. The mean velocity-profile shown in Figure $8(a)$ is in excellent agreement with DNS, especially in the logarithmic region where the PVMS profile is virtually indistinguishable from DNS while the dynamic model, at the same resolution, slightly over predicts the wall shear. The rms statistics for both the dynamic model and PVMS (Figures $8(b) - (d)$) are in good agreement with the unfiltered DNS [30]. Note, that the dynamic model and PVMS simulations use the same domain (see Tables 1) while the DNS uses a slightly larger domain of size $(2\pi, 2, \pi)$. The approximate reduction in computational cost for PVMS compared to the DNS resolution of $384 \times 257 \times 384$ is a factor of nearly 50 times.

To explore the sensitivity of the PVMS results to x-z resolution, the resolution at $Re_\tau = 590$ is reduced to $64 \times 149 \times 64$ while keeping the partition constant at $\overline{N} = 26$ (see Table 1). Figure 9 shows that the mean-velocity profile at the lower resolution is virtually identical to the result at the higher resolution. Similar results for the dynamic model (also shown in figure 9) show that at both resolutions the dynamic model over predicts the wall shear-stress, although it does improve with increased resolution.

Overall, the PVMS results are in excellent quantitative agreement with low-order statistics from DNS at both $Re_\tau = 180$ and 590 and are obtained at a fraction of the computational cost of DNS. PVMS consistently outperforms the dynamic Smagorinsky model yielding results in better agreement with DNS at lower resolutions. In all cases, our planar implementation of VMS gives results similar in quality to the full VMS implementation of Hughes et al. [3]. However, by using fully implicit time-advancement in the wall-normal direction, our implementation is better suited for turbulence control research and we now apply this tool to simulate an opposition control strategy.

Opposition Control

Results for opposition control are presented for friction velocity Reynolds numbers 100, 180, 360, and 590. The quantitative agreement between DNS [9, 11] and the dynamic model [1] for drag reduction at these Reynolds numbers is excellent. Controlled drag histories from PVMS simulations over this range of Reynolds numbers are presented in Figures 10–13 along with the corresponding sensing plane locations y_s^+. The optimal drag reduction and the corresponding location of the sensing plane are estimated by passing a spline (using the Matlab spline function based on a not-a-knot end-condition) through the data shown in Figure 14. The drag reduction of 26% predicted by PVMS for $Re_\tau = 100$ at a sensing plane location of $y_s^+ \approx 16$ is in good agreement with both DNS data obtained using a resolution $(42 \times 65 \times 42)$ and the dynamic model [1]. The maximum drag reduction for $Re_\tau = 180$ of approximately 25% when $y_s^+ \approx 15$ is also in excellent agreement with DNS [9]. Similarly, the quantitative comparison of the PVMS predictions at $Re_\tau = 360$ and 590, seen in Figure 14, are in close correspondence with the well-resolved dynamic model simulations from our prior study [1]. The drag reduction predicted by PVMS for opposition control are summarized in Table 4 along with two measures used to evaluate the control efficiency [1, 26]. In this table, $\mathcal{P}_\mathcal{D}$ is the power saved due to drag reduction, $\mathcal{P}_\phi$ is the power input by the control, and $\mathcal{P}_{|\phi|}$ is a more conservative estimate for power input by the control that does not allow the flow to perform work on the control [26]. Notable trends in Table 4 include the shift of the optimal sensing plane location corresponding to maximum drag-reduction closer to the wall as Re_τ increases and the reduction in control efficiency, as measured by the ratio of power saved to power input, with increased Reynolds number. These trends have been predicted in our recent study using the dynamic model [1] and are verified here using PVMS.

The mean and rms statistics of the controlled flow at $Re_\tau = 180$ (PVMS3) are presented in Figure 15. The controlled statistics from PVMS simulations show the same trends reported by Choi *et al.* [11] using DNS and the dynamic-model opposition-control studies of Prabhu *et al.* [13]. The most dramatic change in the rms statistics of the controlled flow is observed in the wall-normal component that has a local minima at a distance approximately halfway between the sensing plane location and the physical wall. This local minima is the so-called virtual wall first identified by Hammond *et al.* [9]. A more detailed study of the virtual wall by Prabhu *et al.* [13], using a POD analysis, shows that it behaves like a slip-wall which hampers the transport of high momentum fluid towards the wall in the sweep phase of the near-wall cycle and is believed to be the principle mechanism for drag reduction in opposition control. The spanwise velocity fluctuations are generally not altered significantly by the action of control, although there is slight attenuation in the magnitude. To summarize, the effect of opposition control is to attenuate the strength of the turbulence intensity in the near-wall region and to obstruct the near-wall cycle that is responsible for increased skin friction at the wall through the introduction of a so-called virtual wall. Our

PVMS simulations support these observations which are consistent with results from other DNS and LES of opposition control [1, 9, 11, 13].

Finally, the issue of relative efficiency and accuracy of PVMS versus the dynamic model for turbulence control simulations is explored. Consider the results at $Re_\tau = 100$ given in Figure 16 which compares the control results for PVMS and the dynamic model with DNS where it is seen that for a similar resolution, PVMS is slightly more accurate in predicting the location of the optimal sensing plane compared to the dynamic model. The advantage of PVMS is more clear at $Re_\tau = 180$, where the agreement for drag reduction predictions for the PVMS simulations (PVMS3), the higher resolution dynamic model (DYN3), and the available DNS [9] is very good (see Figure 17). Moreover, even at low resolutions, PVMS (i.e. PVMS2) produces reasonable drag predictions that are of the same quality as the slightly higher resolution dynamic model (DYN2). We have seen a similar insensitivity to resolution when using PVMS for the uncontrolled flow simulation (recall Figure 9). Overall, PVMS is found to be more efficient (in terms of resolution requirements) than the dynamic model for all Reynolds number considered. Likewise, at equal resolutions, PVMS produces uncontrolled and controlled results in better agreement with available DNS.

Conclusions

Our planar implementation of the variational multiscale method (PVMS) is shown to be an excellent tool for obtaining quantitatively accurate estimates of drag reduction based on opposition control in turbulent channel flow. In particular, the trends predicted by PVMS confirm our findings (originally obtained using the dynamic Smagorinsky model [1]) that opposition control loses both effectiveness and efficiency as Reynolds number increases. Our findings also indicate that PVMS holds an advantage over the dynamic model in the context of turbulence control, both in terms of computational efficiency and accuracy. The success of VMS lies in the fact that modeling is confined to the smallest of the resolved scales while the large, dynamically important scales are not directly influenced by modeling errors. Based on this success, we are currently extending VMS to flows in complex geometries by utilizing a discontinuous Galerkin framework [4]. In this new method, the partition between large- and small-scales can be readily changed on an element-by-element basis — a capability likely needed for complex flows. Using these tools, we hope to exploit the efficiency, accuracy, and simplicity of the VMS method for simulating and optimizing flow-control strategies for complex turbulence flows.

Acknowledgments

The authors are grateful to Prof. Thomas Bewley of UCSD for allowing us to extend his DNS code to support the LES simulations reported here. The authors have also benefited from discussions with Prof. Thomas Hughes of UT-Austin and his continued enthusiasm for this research is

greatly appreciated. This research has been supported in part by the Texas Advanced Technology Program under Grant No. 003604-0011-2001 and through a Stanford/NASA Center for Turbulence Research summer faculty fellowship to SSC. Computations were performed on a 16 processor SGI Origin 2000 which was partly funded by the NSF SCREMS grant DMS–9872009 and by the Los Alamos National Laboratory Computer Science Institute (LACSI) through LANL contract number 03891-99-23, as part of the prime contract (W-7405-ENG-36) between the Department of Energy and the Regents of the University of California.

References

[1]Yong Chang, S. Scott Collis, and Srinivas Ramakrishnan. Viscous effects in control of near-wall turbulence. *Phys. Fluids*, 14(11):4069–4080, 2002.

[2]Thomas J. R. Hughes, Luca Mazzei, and Kenneth E. Jansen. Large eddy simulation and the variational multiscale method. *Computing and Visualization in Science*, 3:47–59, 2000.

[3]Thomas J. R. Hughes, Assad A. Oberai, and Luca Mazzei. Large eddy simulation of turbulent channel flows by the variational multiscale method. *Phys. Fluids*, 13(6):1755–1754, 2001.

[4]S. Scott Collis. The DG/VMS method for unified turbulence simulation. *AIAA Paper 2002-3124*, 2002.

[5]J. A. Clark and E. Markland. Flow visualization in turbulent boundary layers. *ASCE J. Hydraul. Div.*, 87:1635–1664, 1971.

[6]J. Jimenez and P. Moin. The minimal flow unit in near wall turbulence. *J. Fluid Mech.*, 225:221–240, 1991.

[7]J. Jeong, F. Hussain, W. Schoppa, and J. Kim. Coherent structures near the wall in a turbulent channel flow. *J. Fluid Mech.*, 332:185–214, 1997.

[8]Javier Jiménez and A. Pinelli. The autonomous cycle of near-wall turbulence. *J. Fluid Mech.*, 389:335–59, 1999.

[9]E. P. Hammond, T. R. Bewley, and P. Moin. Observed mechanisms for turbulence attenuation and enhancement in opposition-controlled wall-bounded flows. *Phys. Fluids*, 10(9):2421–2423, 1998.

[10]Mohamed Gad-el-Hak. Introduction to flow control. In Mohamed Gad-el-Hak, Andrew Pollard, and Jean-Paul Bonnet, editors, *Flow Control: Fundamentals and Practices*, pages 199–273. Springer, 1998.

[11]H. Choi, P. Moin, and J. Kim. Active turbulence control for drag reduction in wall-bounded flows. *J. Fluid Mech.*, 262(75):75–110, 1994.

[12]Changhoon Lee, John Kim, David Babcock, and Rodney Goodman. Application of neural networks to turbulence control for drag reduction. *Phys. Fluids*, 9(6):1740–1747, 1997.

[13]R. D. Prabhu, S. Scott Collis, and Yong Chang. The influence of control on proper orthogonal decomposition of wall-bounded turbulent flows. *Phys. Fluids*, 13(2):520–537, 2001.

[14]Yong Chang and S. Scott Collis. Active control of turbulent channel flows based on large eddy simulation. *ASME Paper No. FEDSM-99-6929*, 1999.

[15]S. Scott Collis, Yong Chang, Steven Kellogg, and R. D. Prabhu. Large eddy simulation and turbulence control. *AIAA Paper 2000-2564*, 2000.

[16]Yong Chang. *Reduced Order Methods for Optimal Control of Turbulence*. PhD thesis, Rice University, Mechanical Engineering and Materials Science, 2000.

[17]S. Scott Collis. Monitoring unresolved scales in multiscale turbulence modeling. *Phys. Fluids*, 13(6):1800–1806, 2001.

[18]F. Abergel and R. Temam. On some control problems in fluid mechanics. *Theoretical and Computational Fluid Dynamics*, 1:303–325, 1990.

[19]M. D. Gunzburger, L. S. Hou, and T. P. Svobotny. Optimal control and optimization of viscous, incompressible flows. In M. D. Gunzburger and R. A. Nicolaides, editors, *Incompressible Computational Fluid Dynamics*, pages 109–150, Cambridge, New York, 1993. Cambridge University Press.

[20]Srinivas Ramakrishnan and S. Scott Collis. Partition selection in multi-scale turbulence modeling. *Submitted to Physics of Fluids*, 2003.

[21]Assad A. Oberai and Thomas J. R. Hughes. The variational multiscale formulation of LES: Channel flow at $Re_\tau = 590$. *AIAA 2002-1056*, 2002.

[22]Sandip Ghosal and Parviz Moin. The basic equations for the large-eddy simulation of turbulent flows in complex-geometry. *J. Comp. Phys.*, 118:24–37, 1995.

[23]Massimo Germano, Ugo Piomelli, Parviz Moin, and William H. Cabot. A dynamic subgrid-scale eddy viscosity model. *Phys. Fluids A*, 3(7):1760–1765, 1991.

[24]D. K. Lilly. A proposed modification of the Germano subgrid-scale closure method. *Phys. Fluids A*, 4(3):633–635, 1992.

[25]Knut Akselvoll and Parviz Moin. *Large Eddy Simulation of Turbulent Confined Coannular Jets and Turbulent Flow Over A Backward Facing Step*. PhD thesis, Stanford University, 1995.

[26]Thomas R. Bewley, Parviz Moin, and Roger Teman. DNS-based predictive control of turbulence: an optimal target for feedback algorithms. *J. Fluid Mech.*, 447:179–225, 2001.

[27]C. Canuto, M. Y. Hussaini, A. Quarteroni, and T. A. Zang. *Spectral Methods in Fluid Dynamics*, page 69. Springer-Verlag, 1988.

[28]John Kim, Parviz Moin, and Robert Moser. Turbulence statistics in fully developed channel flow at low Reynolds number. *J. Fluid Mech.*, 177:133–166, 1987.

[29]Srinivas Ramakrishnan. Variational multiscale methods for turbulence control. Master's thesis, Rice University, 2002. Available electronically at http://mems.rice.edu/∼collis.

[30]R. D. Moser, J. Kim, and N. N. Mansour. Direct numerical simulation of turbulent channel flow up to $Re_\tau = 590$. *Phys. Fluids*, 11:943, 1999.

List of Table Captions

Table 1: Simulation parameters used in the uncontrolled-flow, PVMS validation study.

Table 2: Domain and grid resolutions for controlled-flow PVMS simulations.

Table 3: Domain and grid resolutions for controlled-flow dynamic-model simulations.

Table 4: Optimal drag reduction and corresponding power savings ratios at different Reynolds numbers from PVMS simulations.

Re_τ	L_x	L_z	N_x	N_y	N_z	$\overline{N}$	Δx^+	Δy_w^+	Δy_c^+	Δz^+
180	2π	$4\pi/3$	32	33	32	14	35.3	0.93	23.1	23.6
180	2π	$4\pi/3$	32	65	32	14	35.3	0.63	10.5	23.6
180	2π	$4\pi/3$	80	129	96	–	14.1	0.30	5.2	7.9
590	$9\pi/5$	$4\pi/5$	64	149	64	26	52.1	0.59	16.3	23.2
590	$9\pi/5$	$4\pi/5$	72	149	72	26	46.3	0.59	16.3	20.6

TABLE 1:

Case	Re_τ	L_x	L_z	N_x	N_y	N_z	$\overline{N}$	Δx^+	Δy_w^+	Δy_c^+	Δz^+
PVMS1	100	4π	$4\pi/3$	32	49	32	14	39.3	0.47	7.9	13.1
PVMS2	180	4π	$4\pi/3$	36	65	36	14	62.8	0.63	10.5	20.9
PVMS3	180	4π	$4\pi/3$	48	65	48	18	47.1	0.63	10.5	15.7
PVMS4	360	2π	$3\pi/4$	48	97	48	20	47.1	0.58	15.7	17.7
PVMS5	590	$9\pi/5$	$4\pi/5$	72	149	72	26	46.3	0.59	16.3	20.6

TABLE 2:

Case	Re_τ	L_x	L_z	N_x	N_y	N_z	Δx^+	Δy_w^+	Δy_c^+	Δz^+
DYN1	100	4π	$4/3\pi$	32	49	32	39.3	0.47	7.9	13.1
DYN2	180	4π	$4/3\pi$	48	65	48	47.1	0.63	10.5	15.7
DYN3	180	4π	$4/3\pi$	48	65	64	47.1	0.63	10.5	11.8
DYN4	360	2π	$3/4\pi$	48	97	64	47.1	0.58	15.7	13.3
DYN5	590	$9/5\pi$	$4/5\pi$	72	149	96	46.3	0.59	16.3	15.5

TABLE 3:

Case	Re_τ	y_s^+	$\Delta\mathcal{D}\%$	$\mathcal{P}_\mathcal{D}/\mathcal{P}_\phi$	$\mathcal{P}_\mathcal{D}/\mathcal{P}_{\lvert\phi\rvert}$
PVMS1	100	16.07	26.27	269.9	45.3
PVMS2	180	16.01	25.60	105.2	19.1
PVMS3	180	15.26	24.75	99.4	18.0
PVMS4	360	14.36	24.07	77.2	13.5
PVMS5	590	14.05	21.52	66.5	10.9

TABLE 4:

List of Figure Captions

Figure 1: Opposition control schematic.

Figure 2: Near-wall turbulent structures for LES of $Re_\tau = 180$ channel flow: (a) with and (b) without opposition control ($y_s^+ = 16$). Structures are visualized using an iso-surface of negative $\lambda_2 = -0.0055$, the second largest eigenvalue of the velocity gradient tensor [7].

Figure 3: Velocity profiles in wall coordinates for $Re_\tau = 180$: —— DNS, - - - - PVMS, and —·— dynamic model. (a) mean streamwise velocity with ····· law of the wall. (b)–(d) root-mean square velocity components.

Figure 4: Mean-velocity profiles for different resolutions at $Re_\tau = 180$: —— unfiltered DNS, ····· PVMS at $32 \times 33 \times 32$ with $\overline{N} = 14$, - - - - PVMS at $32 \times 65 \times 32$ with $\overline{N} = 14$, —·— coarse grid "DNS" at $32 \times 65 \times 32$.

Figure 5: Root-mean square velocity components for different resolutions at $Re_\tau = 180$: —— unfiltered DNS, ····· PVMS at $32 \times 33 \times 32$ with $\overline{N} = 14$, - - - - PVMS at $32 \times 65 \times 32$ with $\overline{N} = 14$, —·— coarse grid "DNS" at $32 \times 65 \times 32$.

Figure 6: Mean velocity profiles for different partitions at $Re_\tau = 180$ using $32 \times 65 \times 32$: —— DNS, - - - - $\overline{N} = 14$, —·— $\overline{N} = 16$, and ····· $\overline{N} = 18$.

Figure 7: Root-mean square velocity profiles for different partitions at $Re_\tau = 180$ using $32 \times 65 \times 32$: —— DNS, - - - - $\overline{N} = 14$, —·— $\overline{N} = 16$, and ····· $\overline{N} = 18$.

Figure 8: Velocity profiles in wall coordinates for $Re_\tau = 590$: —— DNS (ref. 30), - - - - PVMS, and —·— dynamic model with ($72 \times 149 \times 72$). (a) mean streamwise velocity with ····· law of the wall. (b)–(d) root-mean square velocity components.

Figure 9: Mean-velocity profiles at $Re_\tau = 590$ using different resolutions: - - - - PVMS $64 \times 149 \times 64$ with $\overline{N} = 26$; —·— PVMS $72 \times 149 \times 72$ with $\overline{N} = 26$; —·— dynamic model $64 \times 149 \times 64$; ····· dynamic model $72 \times 149 \times 72$; —— DNS [30].

Figure 10: Drag histories for different sensing plane locations at $Re_\tau = 100$. PVMS1 with a partition $\overline{N} = 14$ using a resolution of ($32 \times 49 \times 32$).

Figure 11: Drag histories for different sensing plane locations at $Re_\tau = 180$. PVMS3 with a partition $\overline{N} = 18$ using a resolution of ($48 \times 65 \times 48$).

Figure 12: Drag histories for different sensing plane locations at $Re_\tau = 360$. PVMS4 with a partition $\overline{N} = 20$ using a resolution of ($48 \times 97 \times 48$).

Figure 13: Drag histories for different sensing plane locations at $Re_\tau = 590$. PVMS5 with a partition $\overline{N} = 26$ using a resolution of ($72 \times 149 \times 72$).

Figure 14: Optimal drag reduction and sensing plane locations: —— PVMS; - - - - dynamic model [1]; —·— DNS at $Re_\tau = 100$ using a resolution of ($42 \times 65 \times 42$). The symbols $\triangle$, $\circ$, $\square$, and $\diamond$ are for $Re_\tau =$ 100, 180, 360, and 590, respectively.

Figure 15: Velocity profiles in wall coordinates for controlled flow: PVMS3 with resolution ($48 \times 65 \times 48$) on the domain ($4\pi, 2, 4/3\pi$); —— PVMS3 (no control); and —·— PVMS3 (control). (a) mean streamwise velocity with ····· law of the wall. (b)–(d) root-mean square velocity components.

Figure 16: Optimal drag reduction and sensing plane locations for $Re_\tau = 100$: —— PVMS1; - - - - DYN1 [1]; and —·— DNS at $Re_\tau = 100$ using a resolution of ($42 \times 65 \times 42$).

Figure 17: Optimal drag reduction and sensing plane locations for $Re_\tau = 180$ using different resolutions: —— PVMS; - - - - dynamic model [1]; • DNS [9, 11].

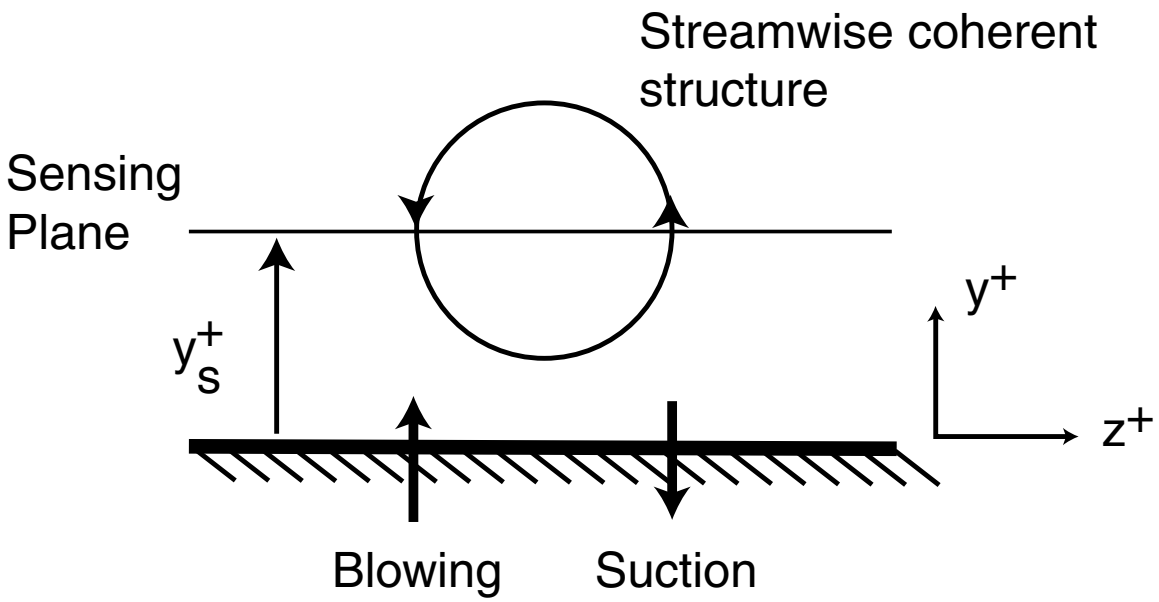
Streamwise coherent
structure
Sensing
Plane
y_s^+
y^+
z^+
Blowing
Suction

FIGURE 1:

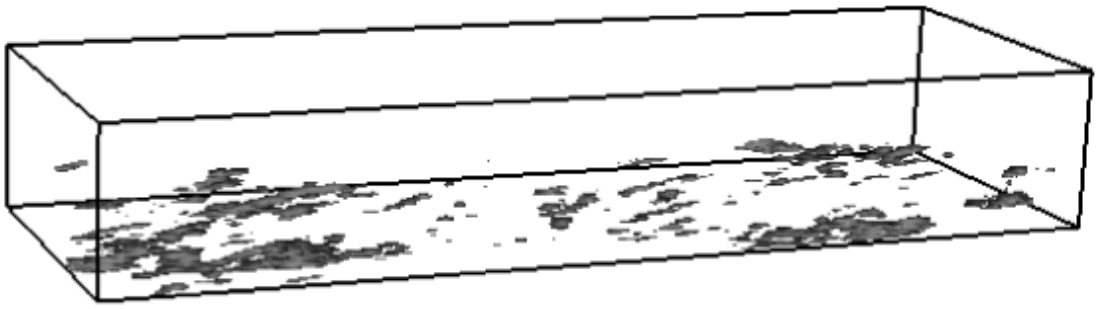

(a) No Control

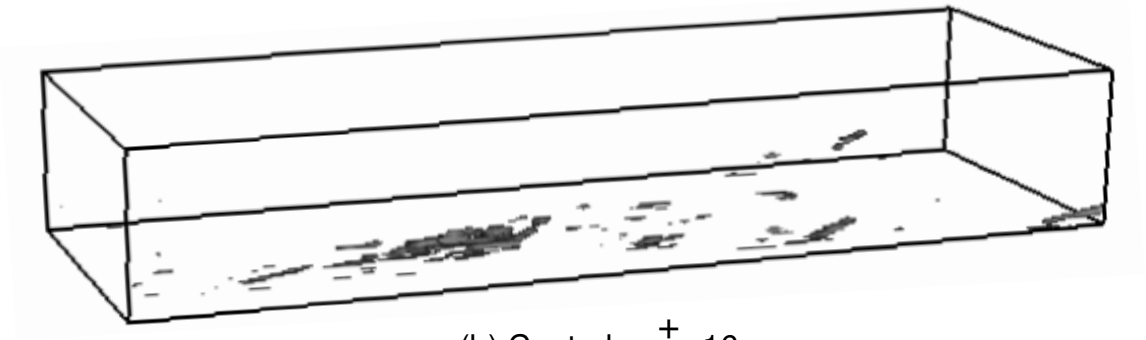

(b) Control, $y_s^+ = 16$

FIGURE 2:

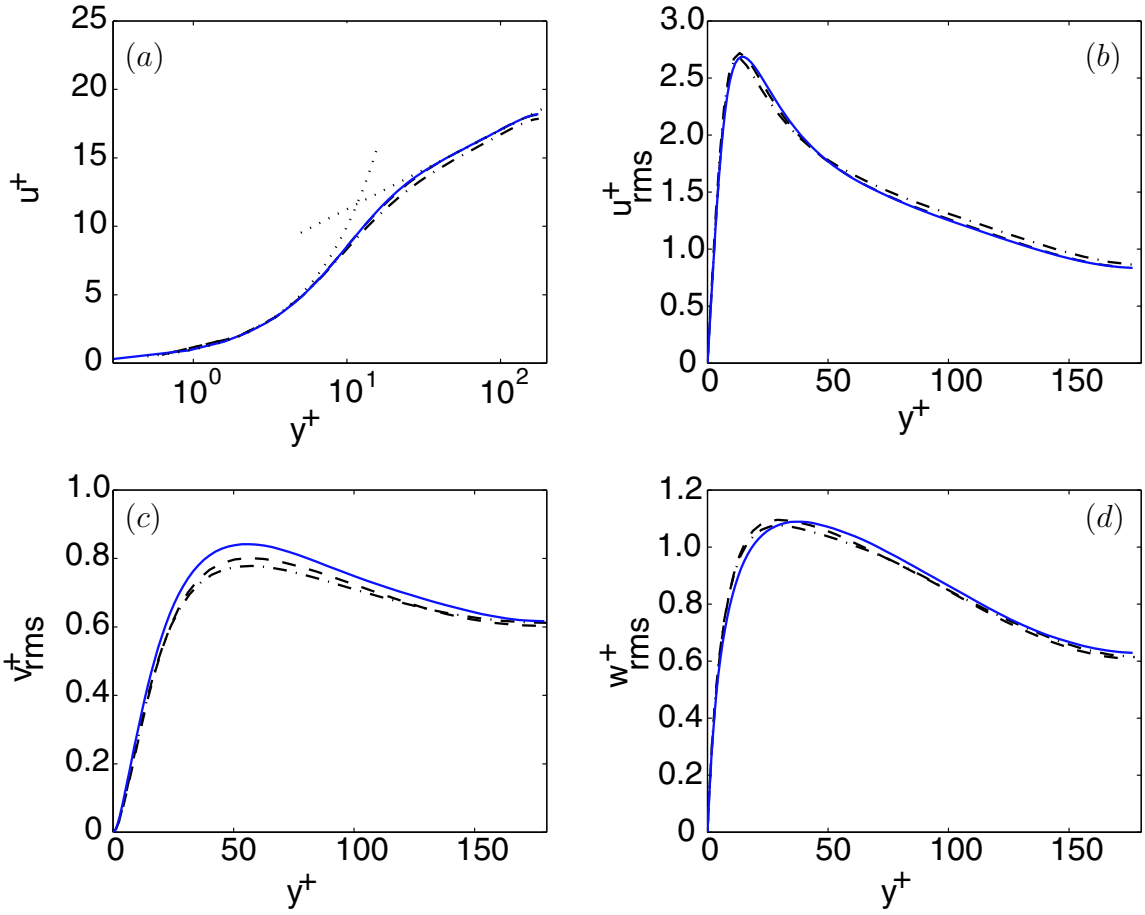

FIGURE 3:

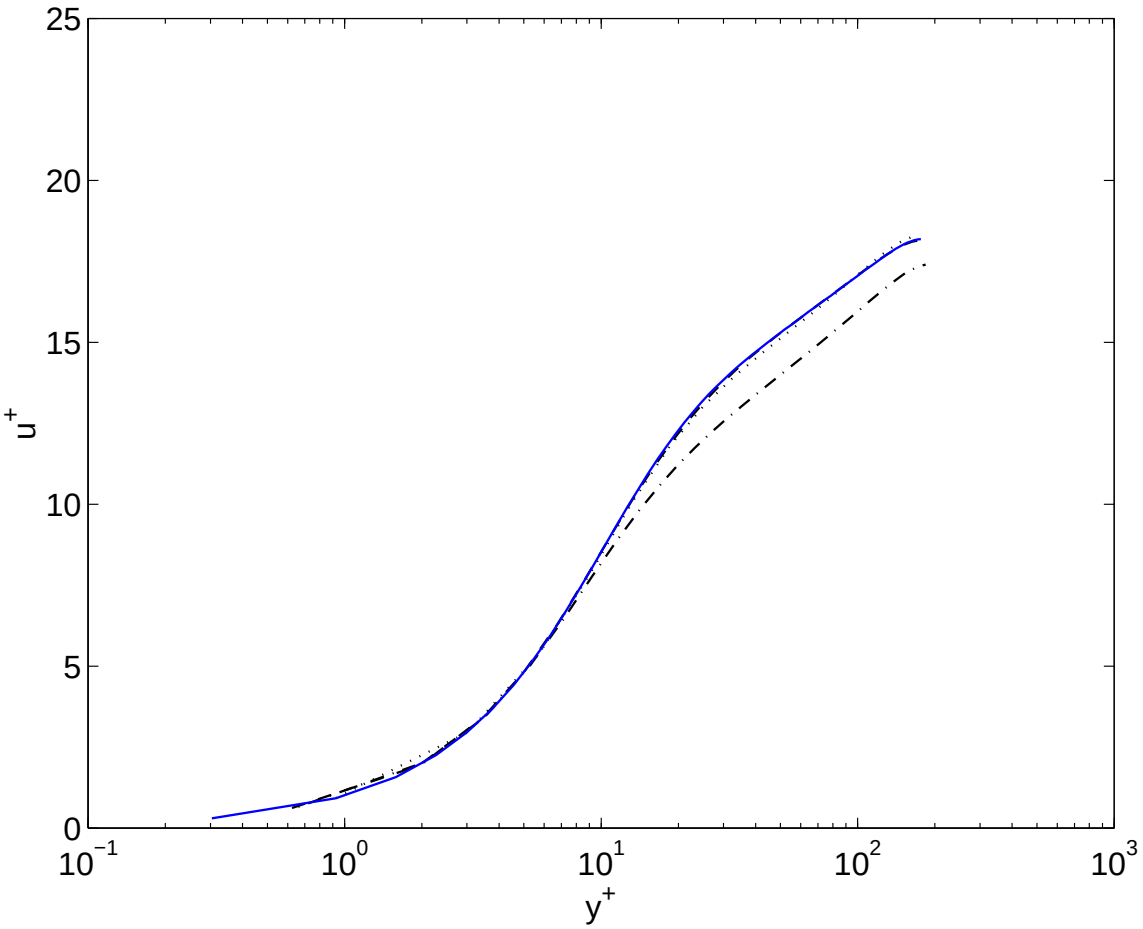

FIGURE 4:

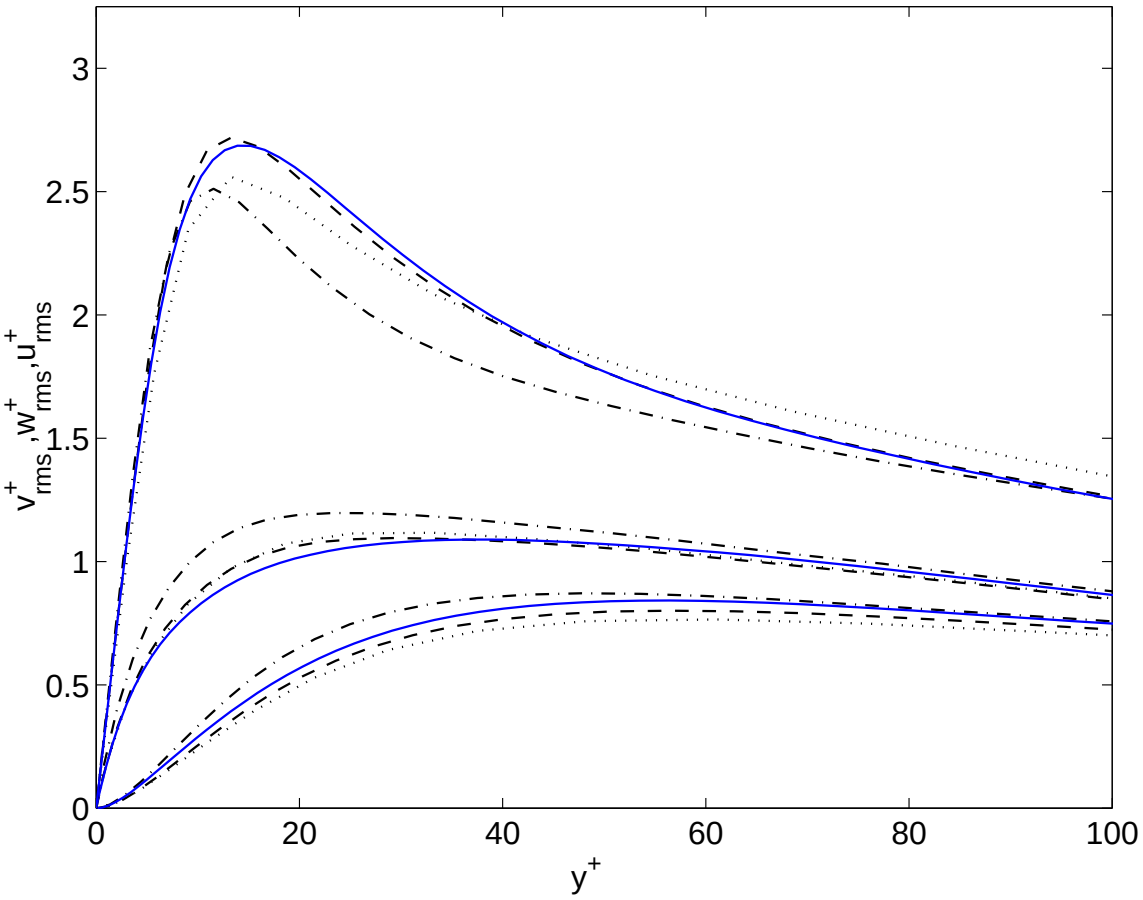

FIGURE 5:

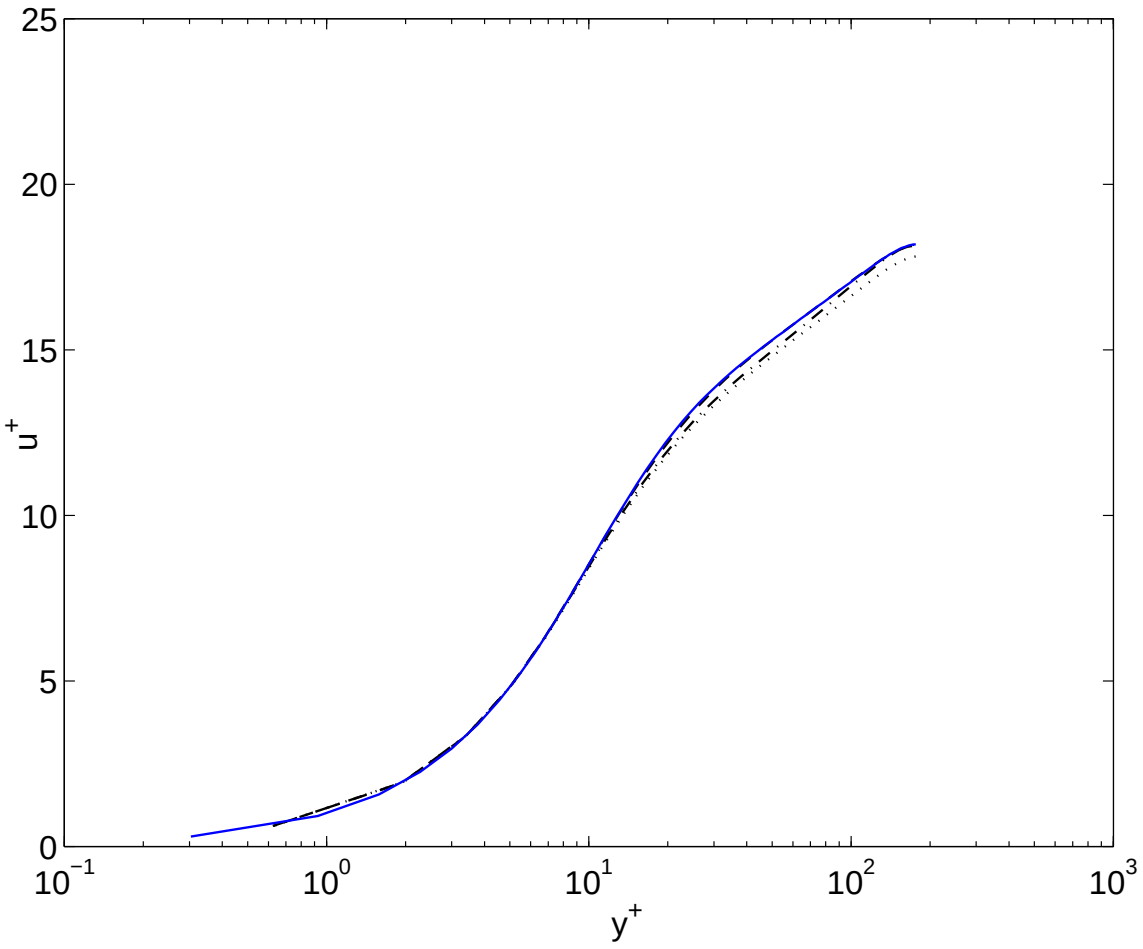

FIGURE 6:

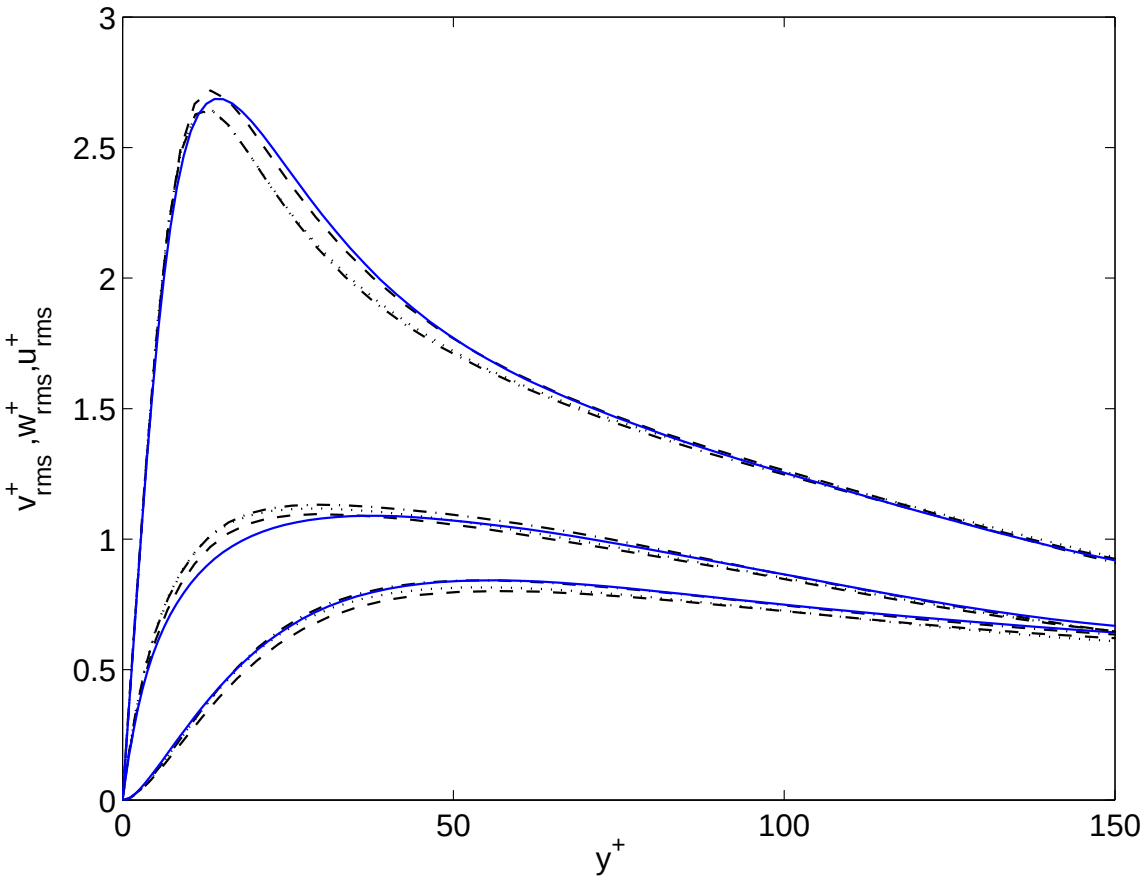

FIGURE 7:

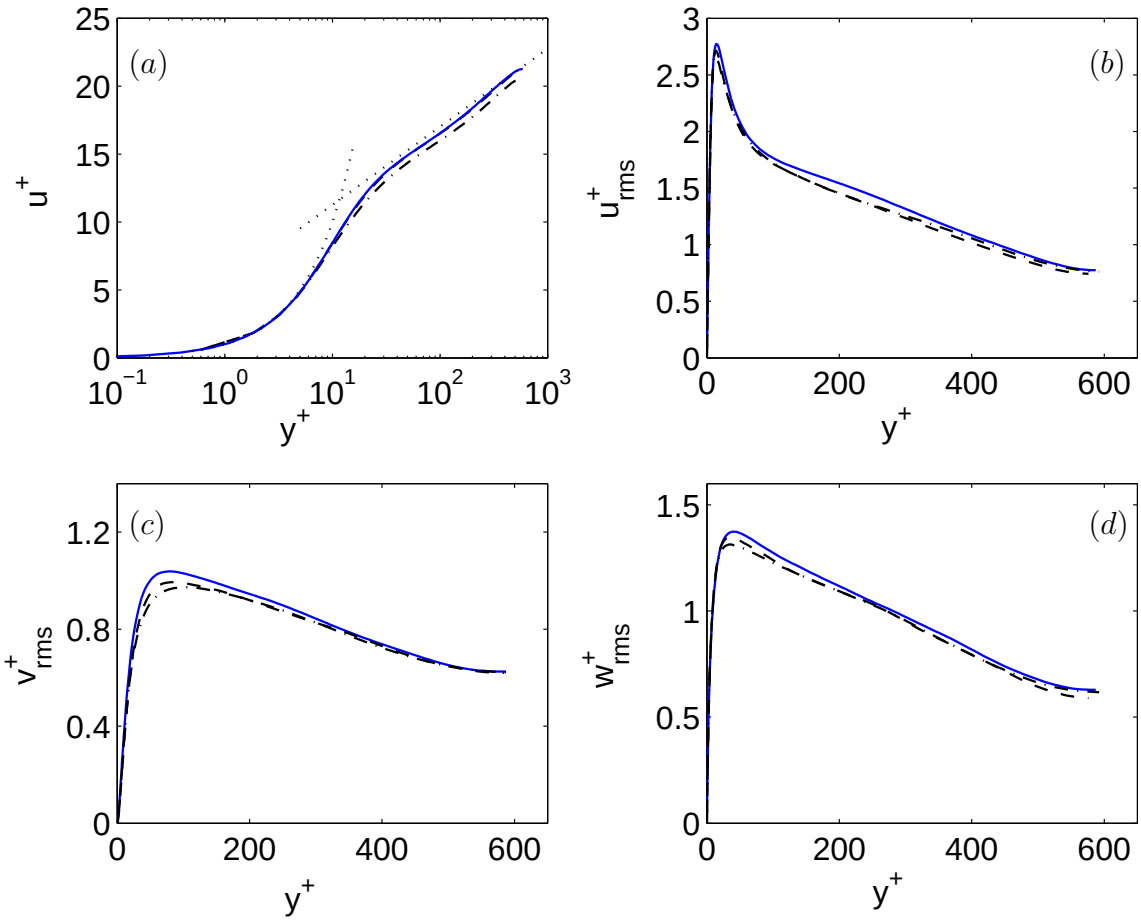
(a)
(b)
(c)
(d)
u+
y+
u+rms
v+rms
w+rms
25
20
15
10
5
0
10−1
100
101
102
103
3
2.5
2
1.5
1
0.5
200
400
600
1.2
0.8
0.4

FIGURE 8:

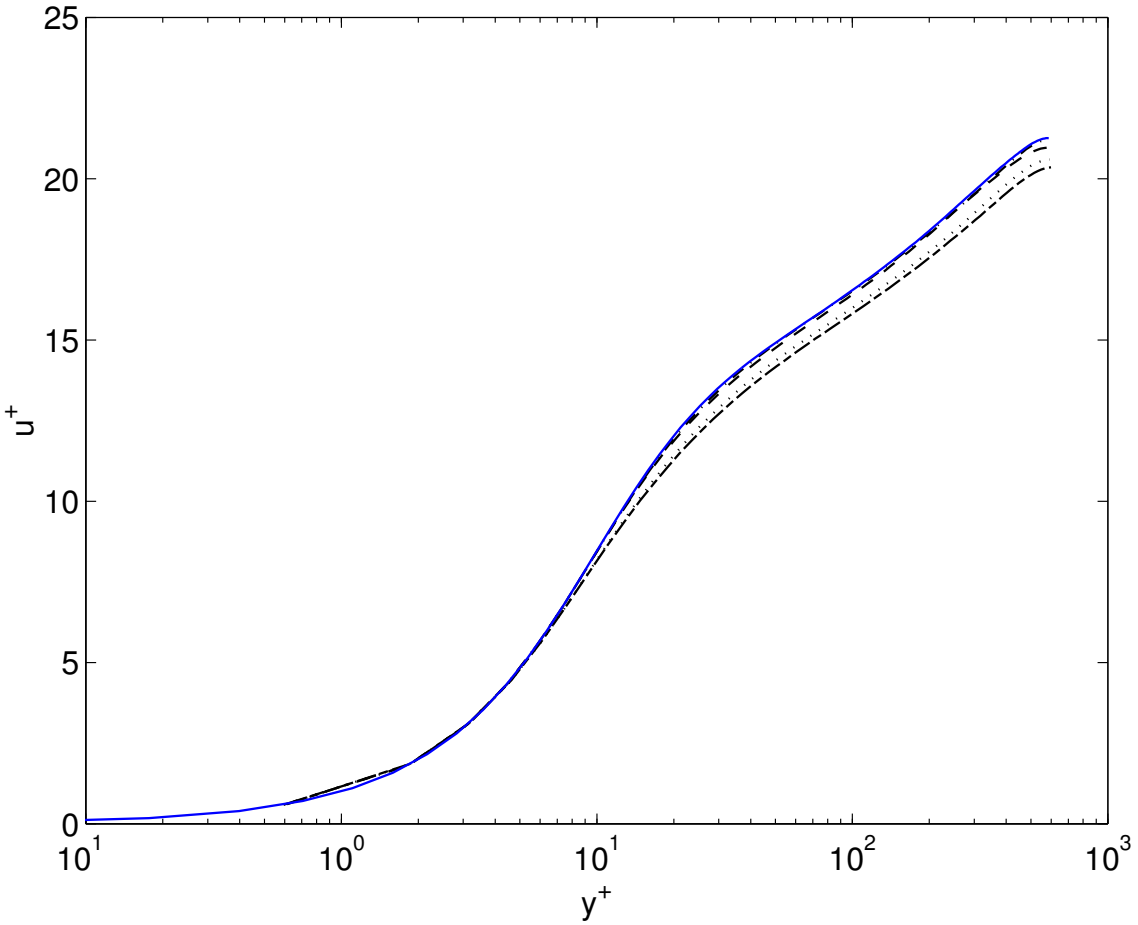

FIGURE 9:

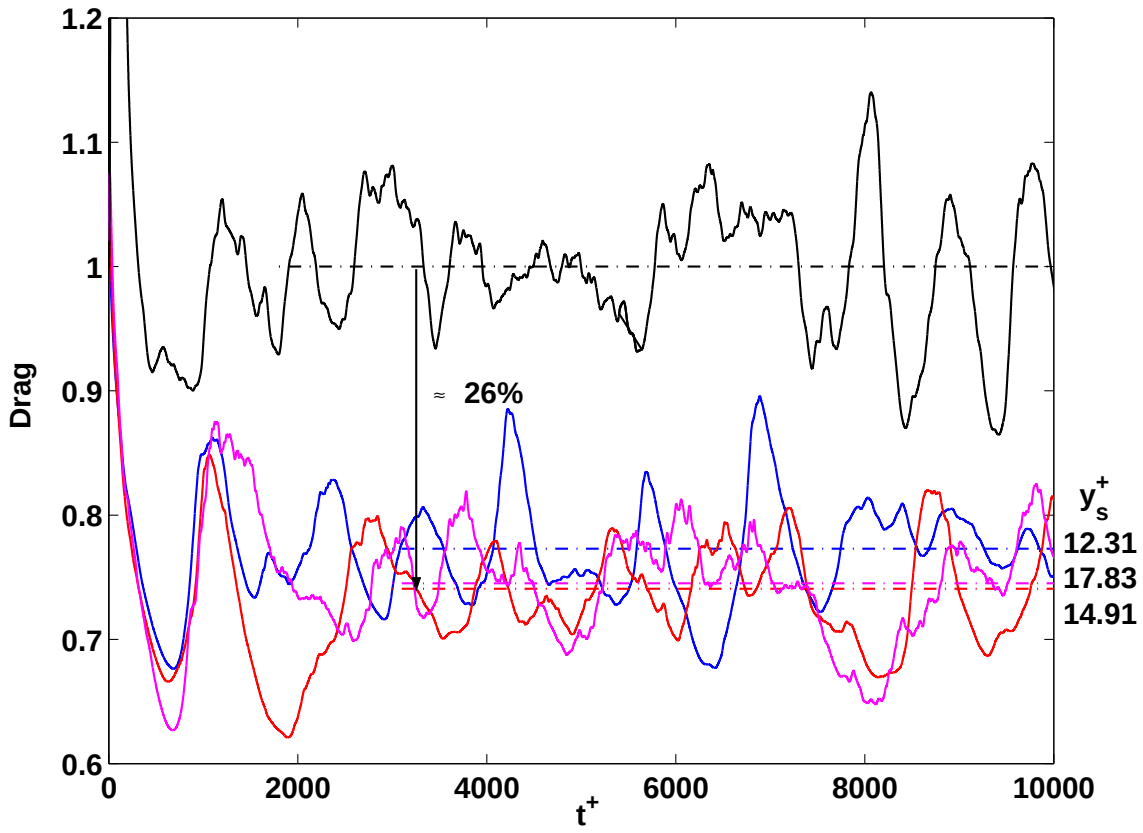
1.2
1.1
1
0.9
0.8
0.7
0.6
Drag
0
2000
4000
6000
8000
10000
t+
≈ 26%
y+s
12.31
17.83
14.91

FIGURE 10:

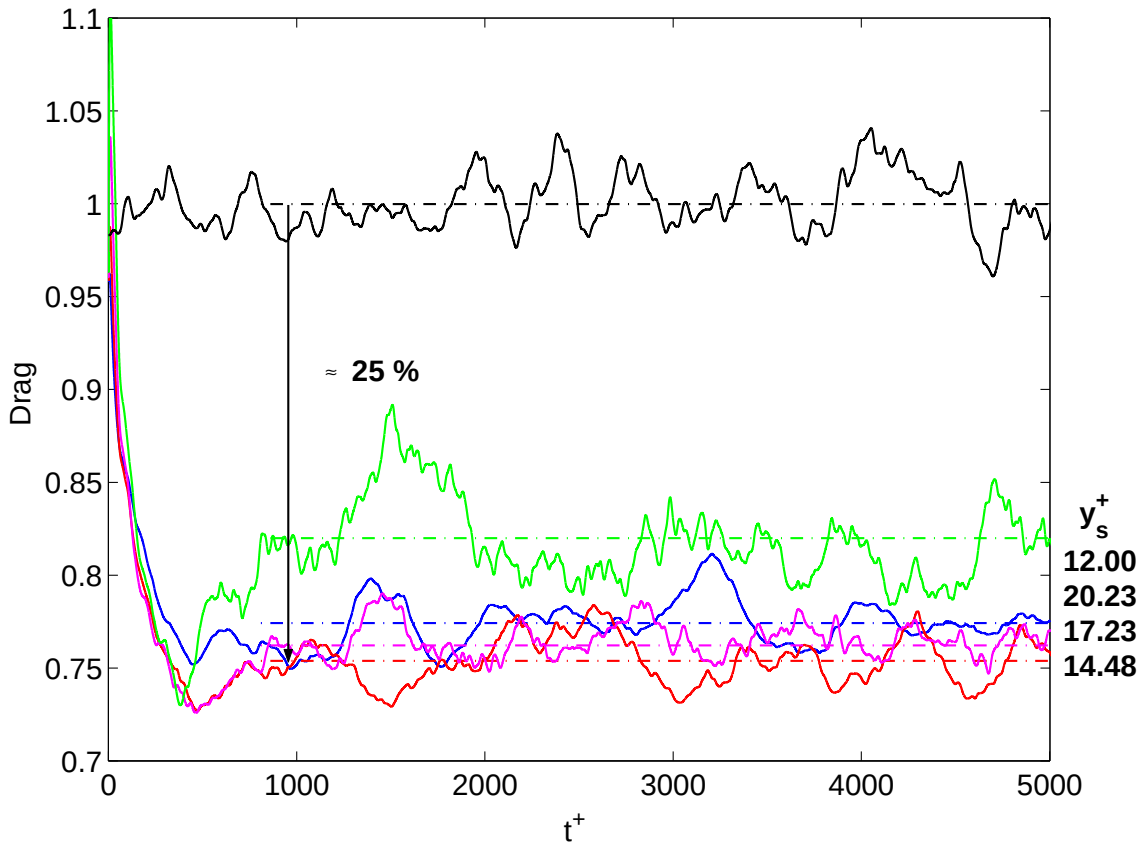
1.1
1.05
1
0.95
0.9
0.85
0.8
0.75
0.7
Drag
0
1000
2000
3000
4000
5000
t+
≈ 25 %
y+s
12.00
20.23
17.23
14.48

FIGURE 11:

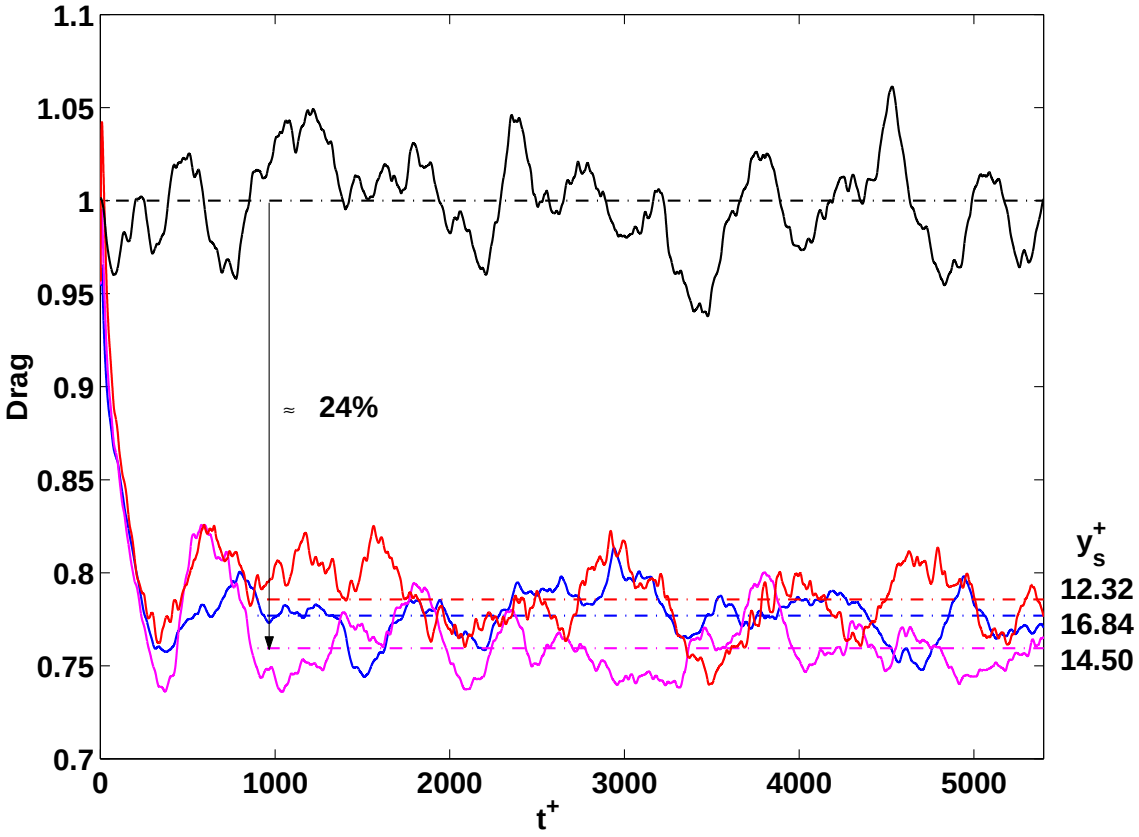
1.1
1.05
1
0.95
0.9
0.85
0.8
0.75
0.7
Drag
≈ 24%
0
1000
2000
3000
4000
5000
t+
y+s
12.32
16.84
14.50

FIGURE 12:

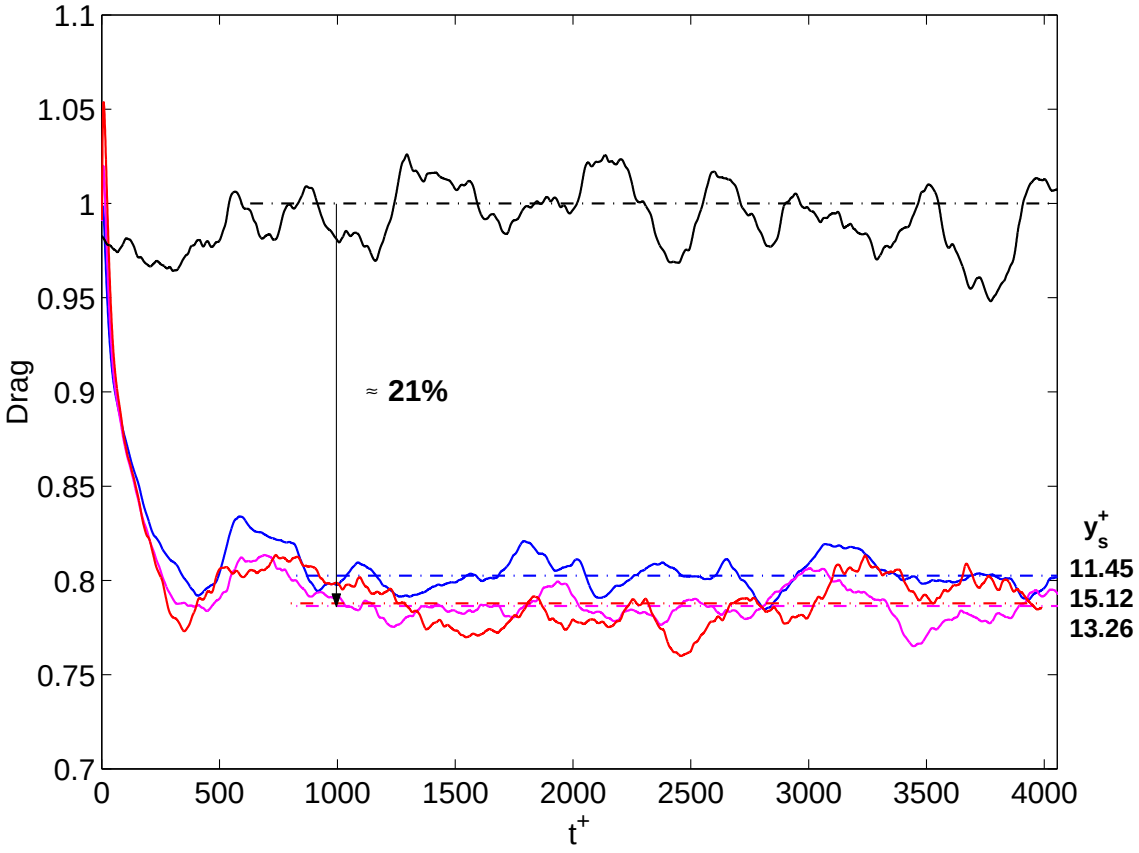
1.1
1.05
1
0.95
0.9
0.85
0.8
0.75
0.7
Drag
0
500
1000
1500
2000
2500
3000
3500
4000
t+
≈ 21%
y+s
11.45
15.12
13.26

FIGURE 13:

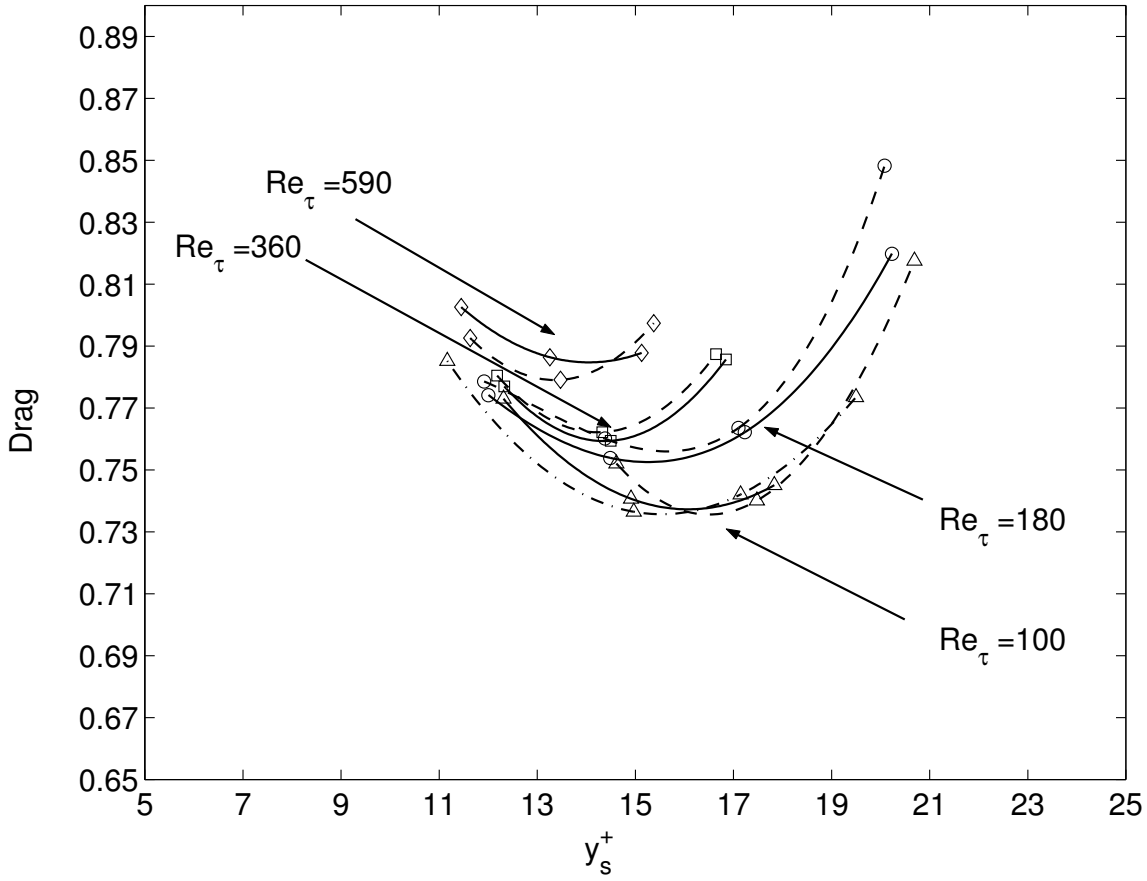
0.89
0.87
0.85
0.83
0.81
0.79
0.77
0.75
0.73
0.71
0.69
0.67
0.65
Drag
5
7
9
11
13
15
17
19
21
23
25
y_s^+
Re_τ =590
Re_τ =360
Re_τ =180
Re_τ =100

FIGURE 14:

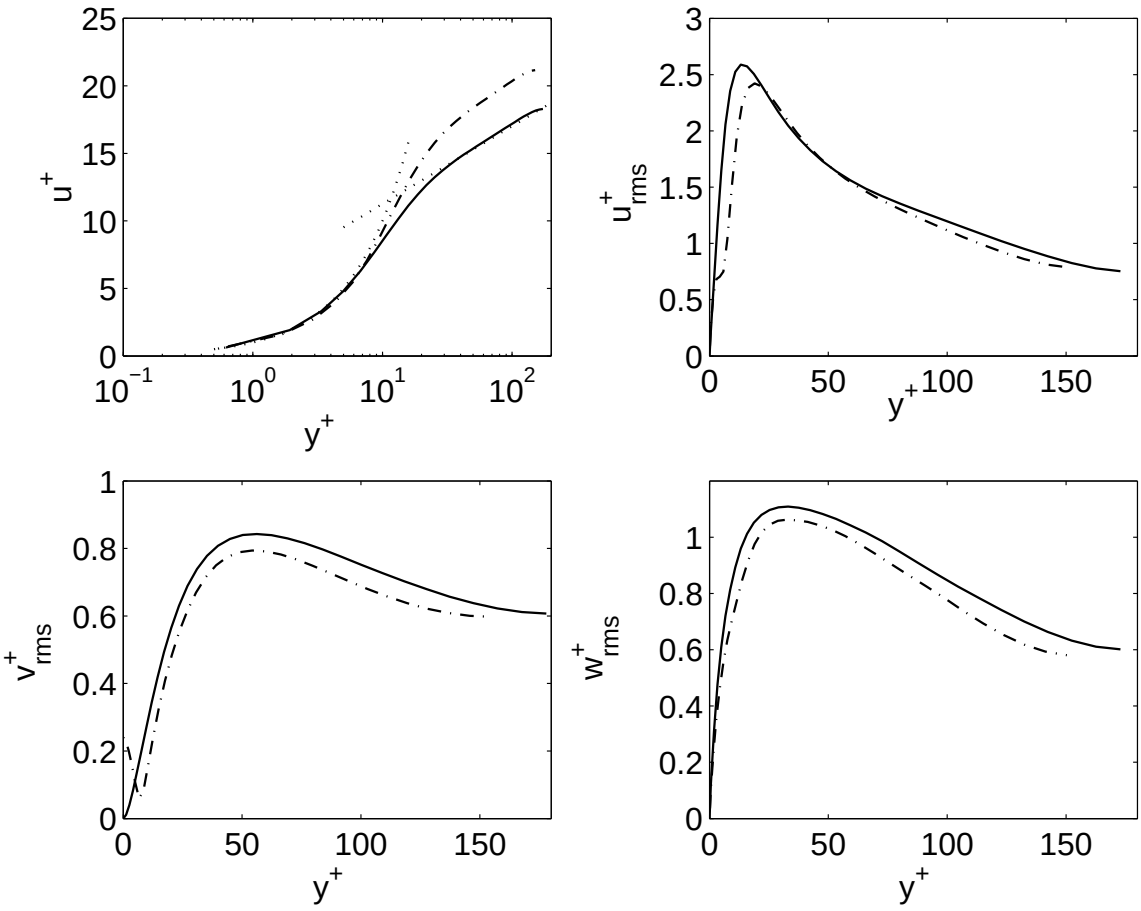
25
20
15
10
5
0
u^+
10^{-1}
10^0
10^1
10^2
y^+
3
2.5
2
1.5
1
0.5
0
u^+_{rms}
0
50
100
150
y^+
1
0.8
0.6
0.4
0.2
0
v^+_{rms}
0
50
100
150
y^+
1
0.8
0.6
0.4
0.2
0
w^+_{rms}
0
50
100
150
y^+

FIGURE 15:

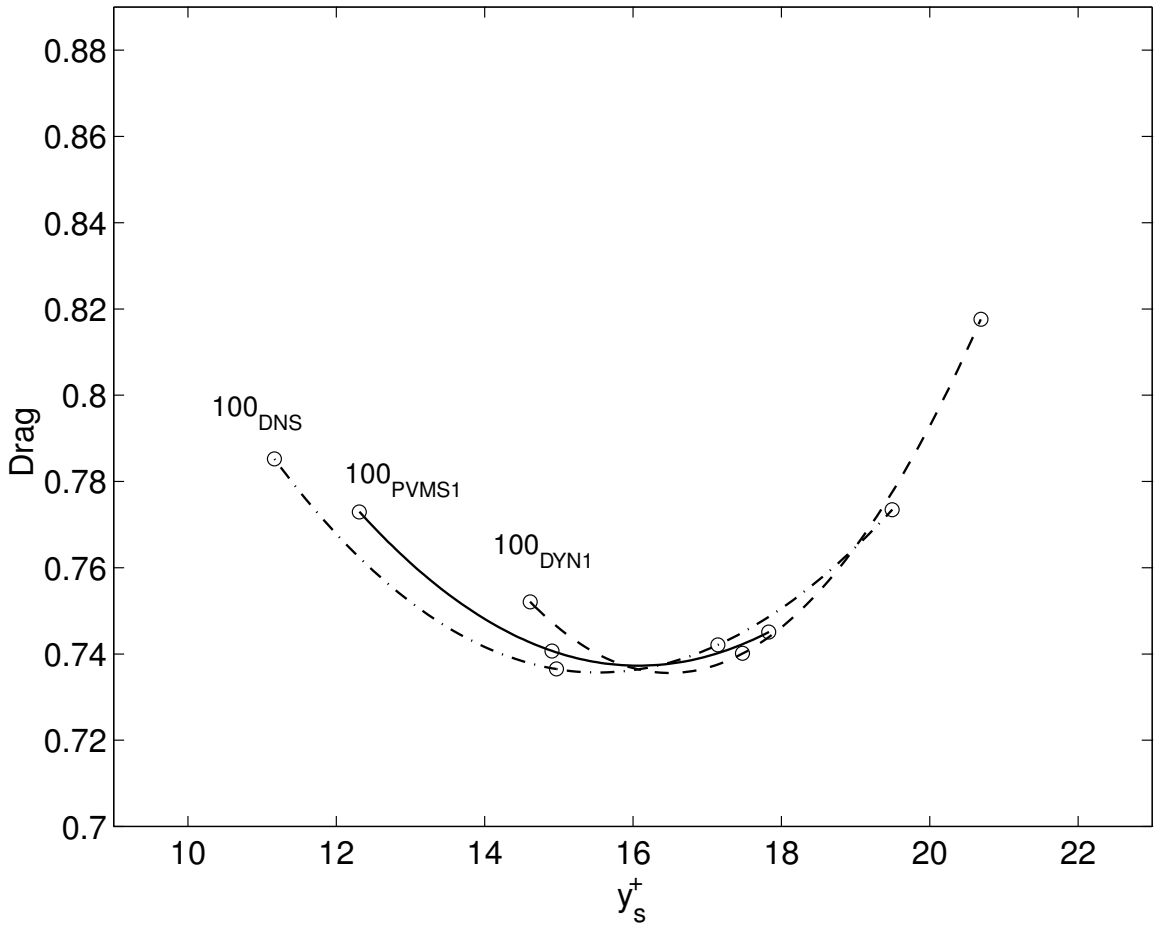
0.88
0.86
0.84
0.82
0.8
0.78
0.76
0.74
0.72
0.7
Drag
10
12
14
16
18
20
22
y_s^+
100_{DNS}
100_{PVMS1}
100_{DYN1}

FIGURE 16:

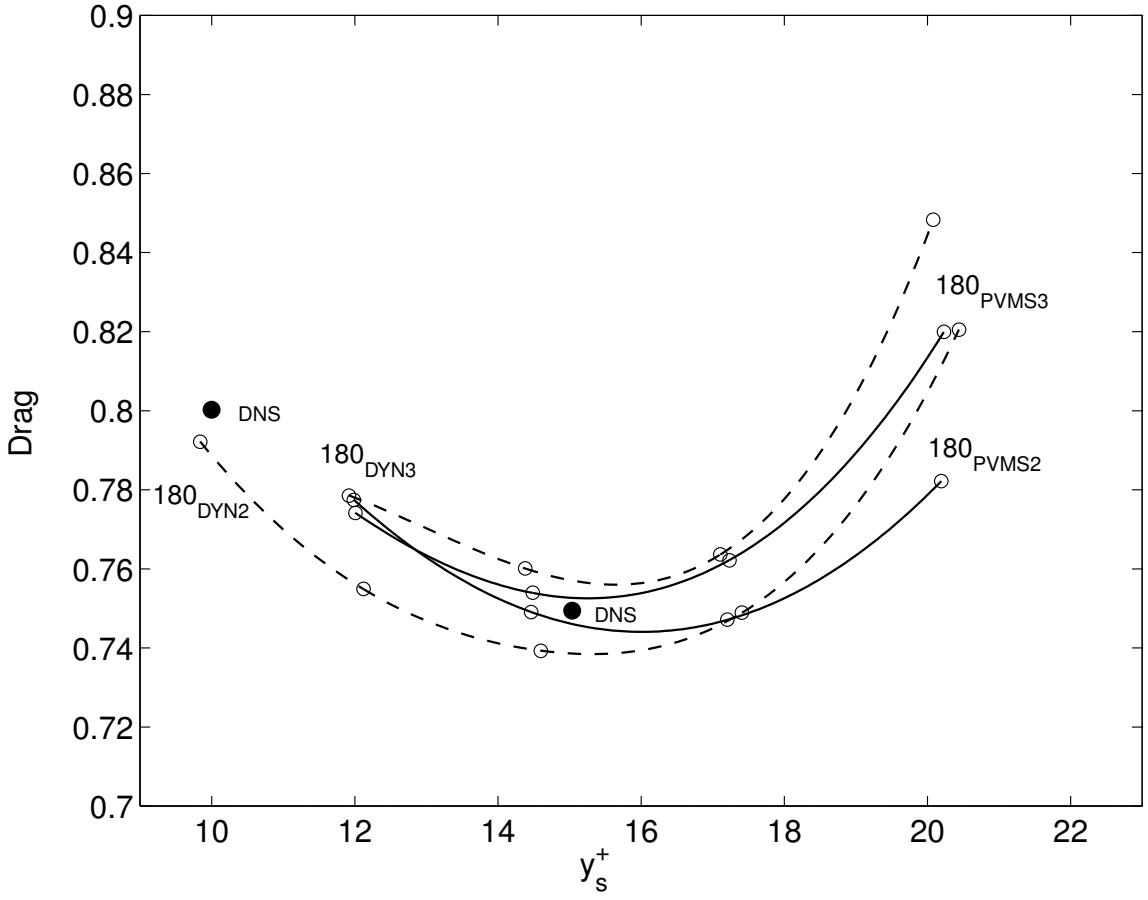
0.9
0.88
0.86
0.84
0.82
0.8
0.78
0.76
0.74
0.72
0.7
Drag
10
12
14
16
18
20
22
y_s^+
DNS
DNS
180_{DYN3}
180_{DYN2}
180_{PVMS3}
180_{PVMS2}

FIGURE 17: